



POLITECNICO
MILANO 1863

[RE.PUBLIC@POLIMI](#)

Research Publications at Politecnico di Milano

Post-Print

This is the accepted version of:

X. Wang, M. Morandini, P. Masarati
Velocity Feedback Damping of Piezo-Actuated Wings
Composite Structures, Vol. 174, 2017, p. 221-232
doi:10.1016/j.compstruct.2017.04.016

The final publication is available at <http://dx.doi.org/10.1016/j.compstruct.2017.04.016>

Access to the published version may require subscription.

When citing this work, cite the original published paper.

© 2017. This manuscript version is made available under the CC-BY-NC-ND 4.0 license
<http://creativecommons.org/licenses/by-nc-nd/4.0/>

Permanent link to this version

<http://hdl.handle.net/11311/1021210>

Velocity feedback damping of piezo-actuated wings

Xiao Wang*, Marco Morandini, Pierangelo Masarati

*Dipartimento di Scienze e Tecnologie Aerospaziali, Politecnico di Milano, Via La Masa 34,
20156 Milano, Italy*

Abstract

A geometrical nonlinear model of thin-walled beams with fiber-reinforced and piezo-composite is developed for smart aircraft wing structures. Some non-classical effects such as warping inhibition and three-dimensional (3-D) strain are accounted for in the beam model. The governing equations and the corresponding boundary conditions are derived using the Hamilton's principle. The Extended Galerkin's Method is used for the numerical study. A negative velocity feedback control algorithm is adopted to control the aircraft wing response. The effective damping performance is optimized by studying anisotropic characteristics of piezo-composite and elastic tailoring of the fiber-reinforced host structure. The relations between active vibration control effect and design factors, such as the size and position of piezo-actuator are investigated in detailed. *Keywords:* thin-walled beam, fiber-reinforced, piezo-composite, active control

Nomenclature

a_{ij}	1-D global stiffness coefficients
\mathcal{A}_i^F	Piezo-actuator coefficients, see Appendix A
b_{ij}	Inertial coefficients
$2b, 2d$	Width and depth of the beam cross-section, see Fig. 1
$B_w, \hat{B}_w, \bar{B}_w$	Pure mechanical bimoment, piezo-bimoment actuation, and

*Corresponding author

Email addresses: xiao.wang@polimi.it (Xiao Wang), marco.morandini@polimi.it (Marco Morandini), pierangelo.masarati@polimi.it (Pierangelo Masarati)

	external bioment on the beam tip
E_i	Electric field intensity
$F_w, a(s)$	Primary and secondary warping functions
k_i	Feed back control gain in Eq. (26)
\hat{h}	Electrode spacing of the interdigitated electrode
L	Length of the beam, see Fig. 1
M_x, M_y, M_z	1-D stress couples of pure mechanical contributions
$\tilde{M}_x, \tilde{M}_y, \tilde{M}_z$	Piezo-moment actuations about the x , y and z axes
$\bar{M}_x, \bar{M}_y, \bar{M}_z$	External stress couples on the beam tip
N	Total number of constituent layers in the wall
N_p, N_h	Numbers of piezocomposite and host layers in the wall
Q_x, Q_z	Shear forces in the x - and z -directions
\tilde{Q}_x, \tilde{Q}_z	Piezo-transverse-shear actuations in the x - and z -directions
\bar{Q}_x, \bar{Q}_z	Applied transverse shear forces at the beam tip
$R(y)$	Distribution function along span for the actuator
(s, y, n)	Local coordinate system on the cross-section, see Fig. 1
$T_y, \tilde{T}_y, \bar{T}_y$	Generalized axial force per unit span, piezo-extension actuation, and applied axial force at the beam tip, respectively
u_0, v_0, w_0	Displacement components of the cross-section along x, y, z axes, see Fig. 1
α_i^k, β_i^k	Weighting coefficients for control gains in Eq. (26)
θ	Ply-angle of layer, see Fig. 1
θ_h, θ_p	Ply-angles of host structure and piezo-actuator
θ_x, θ_z, ϕ	Rotations of the cross-section about the x, z and y axes, see Fig. 1
$\psi(s)$	Torsional function
$\Gamma_t, \tilde{\Gamma}_t$	Pure mechanical nonlinear terms in twist motion and piezo-nonlinear actuation, respectively
δ	Variation operator
$\dot{()}, \ddot{()}, ()'$	$\partial()/\partial t, \partial^2()/\partial t^2, \partial()/\partial y$
\mathbf{X}^T	Transpose of the matrix or vector \mathbf{X}

1. Introduction

Composite thin-walled beams are widely used because of their potential advantages. Among them, light weight, specific high stiffness, and elastic couplings
5 are worth citing. Refined thin-walled beam models have been proposed for open or closed cross-section (see e.g. [1–6]). Among these efforts, Cortinez et al. [3] and Vo and Lee [4] introduced warping shear to improve the model’s accuracy. More generally, any geometrically exact, intrinsic theory of anisotropic beams can be used provided the beam constitutive equation are computed correctly.
10 Many similar approaches, based on a semi-analytical discretization of the beam section displacement field, have been proposed to compute the stiffness matrix of arbitrarily complex beam sections, see e.g. [1, 7, 8]. Basically the same approach can be used for the characterization of composite beams with piezoelectric patches [9, 10]. That said, simplified models such as the one used in
15 this paper are still interesting, as they allow to get a better inside into the dependence of the elastic solution of the beam section parameters.

Piezoelectric material are advantageous because of their fast response. As such, they are well suited for the active control of deformable beams [11–15]. Due to the brittle nature of ceramics, they are however vulnerable to damage and can
20 hardly conform to a curved surface. These drawbacks are overcome by piezo-composite materials such as the Active Fiber Composite (AFC) [16] and the Macro-Fiber Composite (MFC) [17]. Piezo-composite materials can be shaped and bonded to surfaces or embedded into structures. Thanks to their anisotropic characteristics, piezo-composite actuators can produce a twisting actuation that
25 can help controlling the vibration of helicopter blades, see e.g. [18, 19].

In this paper, a geometrical nonlinear thin-walled beam theory incorporating fiber-reinforced and piezo-composite is developed. Transverse shear strain, primary and secondary warping inhibition and three-dimensional strain are accounted for. A typical circumferential asymmetric stiffness (CAS) lay-up con-

30 figuration is adopted to model the aircraft wing structure. The twist-bending elastic coupling induced by the CAS lay-up is beneficial for the aeroelastic response behavior [14, 20, 21], especially for the suppression of the flutter instability [22–24]. Numerical studies based on the Extended Galerkin’s Method are performed, and the relation between actuation performance and voltages is 35 investigated. Based on a negative velocity feedback control algorithm, the dynamic response of an aircraft wing excited by an impulsive load is investigated. Furthermore, the control efficiency is optimized via the study of anisotropic characteristics of piezo-actuator and the elastic tailoring of fiber-reinforced host structure. Finally, considering the high cost and high density of piezo-composite 40 materials, the effect of size and position of the piezo-actuator is investigated.

2. Structural Elements of a Geometrically Nonlinear Theory of Anisotropic Thin-Walled Beams

A geometrical nonlinear, single-cell, closed cross-section, fiber-reinforced composite thin-walled beam model incorporating piezoelectric materials is considered. 45 The geometric configuration and the chosen corresponding coordinate system are indicated in Figs. 1. In addition to the global coordinate (x, y, z) , a local coordinate (s, y, n) is defined on the mid-line contour of the cross-section, see Fig. 1.

2.1. Constitutive relations

We assume that both fiber-reinforced composite material and the piezo-composite material can be modeled with linear piezoelectric constitutive relationships. The constitutive equations of a 3-D piezoelectric continuum can be expressed as [25]

$$\sigma_{ij} = c_{ijkl}^E \varepsilon_{kl} - e_{kij} E_k, \quad (1a)$$

$$D_i = e_{ikl} \varepsilon_{kl} + \kappa_{ik}^\varepsilon E_k, \quad (1b)$$

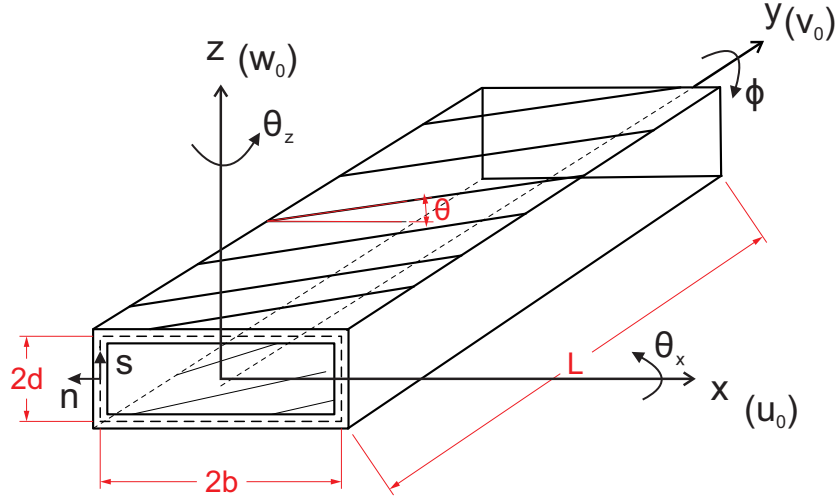


Figure 1: Geometry of the beam with a rectangular cross-section (CAS lay-up).

50 where, c_{ijkl}^E , e_{kij} , and κ_{ik}^ε denote the elastic stiffness coefficients, the piezoelectric stress tensor and the dielectric constant tensor, respectively. The superscripts E and ε denote constant electric field and constant strain, respectively. Symbols σ_{ij} and ε_{kl} denote the stress and strain components, while E_k and D_i denote the electric field intensity and electric displacement vector, respectively.

55 Eq. (1a) describes the *converse piezoelectric effect* which is used for distributed sensing while Eq. (1b) describes the *direct piezoelectric effect* that is used for the active distributed control.

The constitutive equations for the k th layer, reduced to the plane stress condition $\sigma_{nn} = 0$ and referred to the local coordinate system (s, y, n) are

$$\begin{Bmatrix} \sigma_{ss} \\ \sigma_{yy} \\ \tau_{yn} \\ \tau_{sn} \\ \tau_{sy} \end{Bmatrix}_{(k)} = \begin{bmatrix} \bar{Q}_{11} & \bar{Q}_{12} & 0 & 0 & \bar{Q}_{16} \\ \bar{Q}_{12} & \bar{Q}_{22} & 0 & 0 & \bar{Q}_{26} \\ 0 & 0 & \bar{Q}_{44} & \bar{Q}_{45} & 0 \\ 0 & 0 & \bar{Q}_{45} & \bar{Q}_{55} & 0 \\ \bar{Q}_{16} & \bar{Q}_{26} & 0 & 0 & \bar{Q}_{66} \end{bmatrix}_{(k)} \begin{Bmatrix} \varepsilon_{ss} \\ \varepsilon_{yy} \\ \gamma_{yn} \\ \gamma_{sn} \\ \gamma_{sz} \end{Bmatrix}_{(k)} - \begin{Bmatrix} e_{ss} \\ e_{yy} \\ 0 \\ 0 \\ e_{sy} \end{Bmatrix}_{(k)} E_{1(k)}. \quad (2)$$

We assume constant electric field through the actuator thickness, i.e., $E_1 = -(V/\hat{h})$, where V and \hat{h} are the applied voltage and electrode spacing of the

interdigitated electrode for the actuator layer, respectively. And the reduced piezoelectric stress coefficients can be computed as

$$e_{ss} = m^2 e_{11} + n^2 e_{12} - \frac{\bar{C}_{13}}{\bar{C}_{33}} e_{13}, \quad e_{yy} = n^2 e_{11} + m^2 e_{12} - \frac{\bar{C}_{23}}{\bar{C}_{33}} e_{13}, \quad (3a)$$

$$e_{sy} = mn(e_{11} - e_{12}) - \frac{\bar{C}_{36}}{\bar{C}_{33}} e_{13}, \quad (3b)$$

where $m \equiv \cos \theta$ and $n \equiv \sin \theta$, $\theta \in [0, 2\pi]$.

2.2. 2-D Piezoelectric Constitutive Equations

The host structure is assumed composed of N_h layers; the piezo-actuator is composed of N_p piezocomposite layers. The distribution function $R(\cdot)$ of actuators can be given by (see Fig. 2):

$$R_k(n) = H(n - n_{(k-1)}) - H(n - n_{(k)}), \quad (4a)$$

$$R_k(s) = H(s - s_{k1}) - H(s - s_{k2}), \quad (4b)$$

$$R_k(y) = H(y - y_{k1}) - H(y - y_{k2}), \quad (4c)$$

60 where $H(\cdot)$ denotes Heaviside's distribution, while $(n_{(k-1)}, n_{(k)})$, (s_{k1}, s_{k2}) and (y_{k1}, y_{k2}) denote, in sequence, the top and bottom heights of k th piezoelectric layer measured across the beam thickness, its location along the beam circumference and its span location.

Considering the definition of the stretching quantity A_{ij} , of the bending-stretching coupling stiffness quantity B_{ij} and of the thermal and hygric moments D_{ij} ,

$$(A_{ij}, B_{ij}, D_{ij}) = \sum_{k=1}^N \int_{n_{(k-1)}}^{n_{(k)}} \bar{Q}_{ij}^{(k)}(1, n, n^2) \, dn, \quad (N = N_m + N_l), \quad (5)$$

as well as the assumption $N_{ss} = N_{sn} = 0$ [26],

$$(N_{ss}, N_{yy}, N_{sy}, N_{yn}, N_{sn}) = \sum_{k=1}^N \int_{n_{(k-1)}}^{n_{(k)}} (\sigma_{ss}, \sigma_{yy}, \sigma_{sy}, \sigma_{yn}, \sigma_{sn})_{(k)} \, dn, \quad (6a)$$

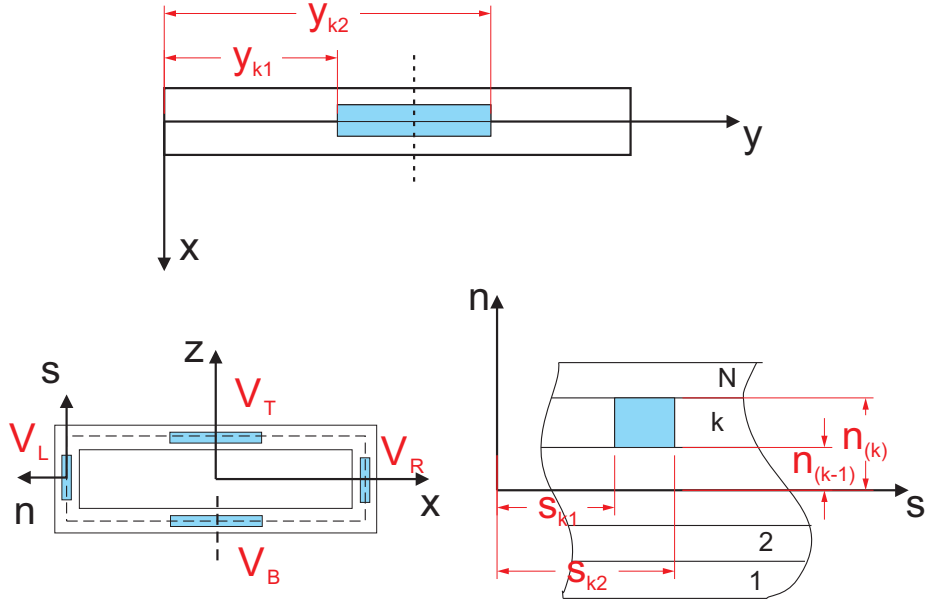


Figure 2: Piezo-actuator location.

$$(L_{yy}, L_{sy}) = \sum_{k=1}^N \int_{n_{(k-1)}}^{n_{(k)}} (\sigma_{yy}, \sigma_{sy})_{(k)} n \, dn, \quad (6b)$$

the stress resultants and stress couples reduce to the following expressions

$$\begin{Bmatrix} N_{yy} \\ N_{ys} \\ L_{yy} \\ L_{sy} \end{Bmatrix} = \begin{bmatrix} K_{11} & K_{12} & K_{13} & K_{14} \\ K_{21} & K_{22} & K_{23} & K_{24} \\ K_{41} & K_{42} & K_{43} & K_{44} \\ K_{51} & K_{52} & K_{53} & K_{54} \end{bmatrix} \begin{Bmatrix} \epsilon_{yy}^0 \\ \gamma_{ys}^0 \\ \phi' \\ \epsilon_{yy}^1 \end{Bmatrix} - \begin{Bmatrix} \tilde{N}_{yy} \\ \tilde{N}_{sy} \\ \tilde{L}_{yy} \\ \tilde{L}_{sy} \end{Bmatrix}, \quad (7)$$

and

$$N_{yn} = \left(A_{44} - \frac{A_{45}^2}{A_{55}} \right) \gamma_{yn}. \quad (8)$$

In these equations, (1) K_{ij} , (2) ϵ_{yy}^0 , (3) ϵ_{yy}^1 , (4) γ_{ys}^0 and (5) γ_{yn} denote (1) the modified local stiffness coefficients, (2) the axial strain associated with the primary warping, (3) a measure of curvature associated with the secondary warping, (4) the tangential shear strain and (5) the transverse shear strain, respectively. Their expressions can be found in Ref. [26]. The piezo-actuator

induced stress resultants \tilde{N}_{yy} , \tilde{N}_{sy} and stress couples \tilde{L}_{yy} , \tilde{L}_{sy} are defined as

$$\begin{cases} \tilde{N}_{yy} = \sum_{k=1}^{N_p} \left(e_{yy} - \frac{A_{12}}{A_{11}} e_{ss} \right) E_{1(k)} [n_{(k)} - n_{(k-1)}] R_{(k)}(s) R_{(k)}(y) \\ \tilde{N}_{sy} = \sum_{k=1}^{N_p} \left(e_{sy} - \frac{A_{16}}{A_{11}} e_{ss} \right) E_{1(k)} [n_{(k)} - n_{(k-1)}] R_{(k)}(s) R_{(k)}(y) \\ \tilde{L}_{yy} = \sum_{k=1}^{N_p} \left[\frac{1}{2} e_{yy} [n_{(k)} + n_{(k-1)}] - \frac{B_{12}}{A_{11}} e_{ss} \right] E_{1(k)} [n_{(k)} - n_{(k-1)}] R_{(k)}(s) R_{(k)}(y) \\ \tilde{L}_{sy} = \sum_{k=1}^{N_p} \left[\frac{1}{2} e_{sy} [n_{(k)} + n_{(k-1)}] - \frac{B_{16}}{A_{11}} e_{ss} \right] E_{1(k)} [n_{(k)} - n_{(k-1)}] R_{(k)}(s) R_{(k)}(y) \end{cases} \quad (9)$$

3. Formulation of the Governing System

Hamilton's principle is used to derive the governing equations and the corresponding boundary conditions. The path of motion renders the following variational form stationary:

$$\int_{t_1}^{t_2} (\delta T + \delta V - \overline{\delta W_e}) dt = 0, \quad (10a)$$

with (at $t = t_1, t_2$)

$$\delta u_0 = \delta v_0 = \delta w_0 = \delta \theta_x = \delta \theta_z = \delta \phi = 0, \quad (10b)$$

65 where T , V and $\overline{\delta W_e}$ denote the kinetic energy, strain energy and the virtual work due to the external forces, respectively.

3.1. Governing Equations

After lengthy variation manipulations, the governing equations are

$$\begin{aligned} \delta u_0 : [(T_y + \tilde{T}_y)u'_0 - (M_z + \tilde{M}_z)\phi' \sin \phi + (M_x + \tilde{M}_x)\phi' \cos \phi \\ + (Q_x + \tilde{Q}_x) \cos \phi + (Q_z + \tilde{Q}_z) \sin \phi]' + p_x - b_1 \ddot{u}_0 = 0, \end{aligned} \quad (11a)$$

$$\delta v_0 : (T_y + \tilde{T}_y)' + p_y - b_1 \ddot{v}_0 = 0, \quad (11b)$$

$$\begin{aligned} \delta w_0 : [(T_y + \tilde{T}_y)w'_0 - (M_z + \tilde{M}_z)\phi' \cos \phi - (M_x + \tilde{M}_x)\phi' \sin \phi \\ - (Q_x + \tilde{Q}_x) \sin \phi + (Q_z + \tilde{Q}_z) \cos \phi]' + p_z - b_1 \ddot{w}_0 = 0, \end{aligned} \quad (11c)$$

$$\begin{aligned}
\delta\phi : & (M_y + \tilde{M}_y)' - (B_w + \tilde{B}_w)'' + [(M_x + \tilde{M}_x)(u'_0 \cos \phi - w'_0 \sin \phi) \\
& - (M_z + \tilde{M}_z)(w'_0 \cos \phi + u'_0 \sin \phi) + (\Gamma_t + \tilde{\Gamma}_t)\phi']' \\
& + (M_x + \tilde{M}_x)(u'_0 \phi' \sin \phi + w'_0 \phi' \cos \phi) \\
& - (M_z + \tilde{M}_z)(w'_0 \phi' \sin \phi - u'_0 \phi' \cos \phi) \\
& + (Q_x + \tilde{Q}_x)(u'_0 \sin \phi + w'_0 \cos \phi) \\
& - (Q_z + \tilde{Q}_z)(u'_0 \cos \phi - w'_0 \sin \phi) \\
& + m_y + b'_w - (b_4 + b_5)\ddot{\phi} + (b_{10} + b_{18})\ddot{\phi}'' = 0,
\end{aligned} \tag{11d}$$

$$\delta\theta_x : (M_x + \tilde{M}_x)' - (Q_z + \tilde{Q}_z) + m_x - b_4\ddot{\theta}_x = 0, \tag{11e}$$

$$\delta\theta_z : (M_z + \tilde{M}_z)' - (Q_x + \tilde{Q}_x) + m_z - b_5\ddot{\theta}_z = 0, \tag{11f}$$

where p_x , p_y and p_z are the external forces per unit span length and m_x , m_y and m_z are the moments about x -, y - and z -axes, respectively; b_w stands for the bimoment of the surface traction. The essential and natural boundary conditions are:

$$\begin{aligned}
\delta u_0 : u_0 = \bar{u}_0 \quad \text{or} \\
T_y u'_0 - M_z \phi' \sin \phi + M_x \phi' \cos \phi + Q_x \cos \phi + Q_z \sin \phi = \bar{Q}_x,
\end{aligned} \tag{12a}$$

$$\delta v_0 : v_0 = \bar{v}_0 \quad \text{or} \quad T_y = \bar{T}_y, \tag{12b}$$

$$\begin{aligned}
\delta w_0 : w_0 = \bar{w}_0 \quad \text{or} \\
T_y w'_0 - M_z \phi' \cos \phi - M_x \phi' \sin \phi - Q_x \sin \phi + Q_z \cos \phi = \bar{Q}_z,
\end{aligned} \tag{12c}$$

$$\begin{aligned}
\delta\phi : \phi = \bar{\phi} \quad \text{or} \\
- B'_w + M_y + M_x(u'_0 \cos \phi - w'_0 \sin \phi) \\
- M_z(w'_0 \cos \phi + u'_0 \sin \phi) + \Gamma_t \phi' + \tilde{\Gamma}_t \phi' = \bar{M}_y - (b_{10} + b_{18})\ddot{\phi}',
\end{aligned} \tag{12d}$$

$$\delta\phi' : \phi' = \bar{\phi}' \quad \text{or} \quad B_w = \bar{B}_w, \quad (12e)$$

$$\delta\theta_x : \theta_x = \bar{\theta}_x \quad \text{or} \quad M_x = \bar{M}_x, \quad (12f)$$

$$\delta\theta_z : \theta_z = \bar{\theta}_z \quad \text{or} \quad M_z = \bar{M}_z. \quad (12g)$$

In Eqs. (11) and (12), the terms without and with over-tilde ($\tilde{\cdot}$) identify the pure mechanical and piezo-actuator contributions, respectively. The expressions
70 for stress and stress couple resultants (e.g. T_y , \tilde{T}_y , M_x , etc.) will be discussed in the following section. Explicit expressions for inertial terms b_{ij} can be found in the appendix of Ref. [26].

4. Governing equation system for circumferential asymmetric stiffness lay-up configuration

75

4.1. Force-displacement relationship

The linearized beam constitutive law reads

$$\mathcal{F}_i = a_{ij}\mathcal{D}_j \quad (13)$$

where \mathcal{F}_i , a_{ij} and \mathcal{D}_j denotes the stress and couple stress resultants (i.e. the beam internal actions), the stiffness coefficients and the beam deformation measure work-conjugated to the internal actions, respectively; see e.g. Ref. [26] for an explicit expression of a_{ij} . The stiffness matrix $[a_{ij}]$ is fully populated in the general case, so that bending, twisting, extension, transverse shearing and warping are all coupled together. For a circumferential asymmetric stiffness (CAS) lay-up configuration the stiffness matrix $[a_{ij}]$ can be decoupled into two types

of elastic coupling, viz, extension-transverse shear

$$\begin{Bmatrix} T_y \\ Q_x \\ Q_z \\ \Gamma_t \end{Bmatrix} = \begin{bmatrix} a_{11} & a_{14} & a_{15} & a_{18} \\ a_{14} & a_{44} & 0 & a_{48} \\ a_{15} & 0 & a_{55} & 0 \\ a_{18} & a_{48} & 0 & a_{88} \end{bmatrix} \begin{Bmatrix} v'_0 + \frac{1}{2}(u'_0)^2 + \frac{1}{2}(w'_0)^2 \\ \theta_z + u'_0 \cos \phi - w'_0 \sin \phi \\ \theta_x + u'_0 \sin \phi + w'_0 \cos \phi \\ \frac{1}{2}(\phi')^2 \end{Bmatrix}, \quad (14a)$$

and bending-twist coupling,

$$\begin{Bmatrix} M_z \\ M_x \\ B_w \\ M_y \end{Bmatrix} = \begin{bmatrix} a_{22} & 0 & 0 & 0 \\ 0 & a_{33} & 0 & a_{37} \\ 0 & 0 & a_{66} & 0 \\ 0 & a_{37} & 0 & a_{77} \end{bmatrix} \begin{Bmatrix} \theta'_z - w'_0 \phi' \cos \phi - u'_0 \phi' \sin \phi \\ \theta'_x + u'_0 \phi' \cos \phi - w'_0 \phi' \sin \phi \\ \phi'' \\ \phi' \end{Bmatrix}; \quad (14b)$$

the stiffness coefficient a_{15} is equal to zero for balanced lay-ups on the left and right beam spars.

4.2. Force-voltage relationship

We introduce two actuator pairs, viz., flange-actuator-pair (top and bottom plates) and web-actuator-pair (left and right spars). Thus, four voltage parameters V_T , V_B , V_L and V_R can be defined, i.e. the voltages applied on the actuators located at the top, bottom, left and right plates of the beam, see Fig. 2. The relation between the piezo-actuator induced stress and stress couple resultants ($\tilde{\mathbf{F}}$) and the voltages (\mathbf{V}) can be expressed as

$$\tilde{\mathbf{F}} = [\mathcal{A}_i^F] R(y) \mathbf{V}, \quad (15)$$

80 where $R(y)$ of Eq. (4c) denotes the location along span of the actuator, $\tilde{\mathbf{F}} = \{\tilde{T}_y \ \tilde{M}_y \ \tilde{B}_w \ \tilde{\Gamma}_t \ \tilde{M}_z \ \tilde{M}_x \ \tilde{Q}_x \ \tilde{Q}_z\}^T$ and $\mathbf{V} = \{V_1 \ V_2 \ V_3 \ V_4\}^T = \frac{1}{2}\{(V_T - V_B) \ (V_T + V_B) \ (V_L - V_R) \ (V_L + V_R)\}^T$. The piezo-actuator coefficients \mathcal{A}_i^F ($i = 1, 2, 3, 4$) are defined in Appendix A.

If the piezo-composite actuators are distributed in CAS configuration, Eq. (15)

can be split in two, viz., extension-transverse coupling

$$\begin{pmatrix} \tilde{T}_y(y, t) \\ \tilde{Q}_x(y, t) \\ \tilde{Q}_z(y, t) \\ \tilde{\Gamma}_t(y, t) \end{pmatrix} = \begin{bmatrix} \mathcal{A}_2^{Ty} & \mathcal{A}_4^{Ty} \\ \mathcal{A}_2^{Qx} & 0 \\ 0 & \mathcal{A}_4^{Qz} \\ \mathcal{A}_2^{\Gamma t} & \mathcal{A}_4^{\Gamma t}(t) \end{bmatrix} \begin{pmatrix} V_2(t) \\ V_4(t) \end{pmatrix} R(y), \quad (16a)$$

and bending-twist coupling

$$\begin{pmatrix} \tilde{M}_z(y, t) \\ \tilde{M}_x(y, t) \\ \tilde{B}_w(y, t) \\ \tilde{M}_y(y, t) \end{pmatrix} = \begin{bmatrix} 0 & \mathcal{A}_3^{Mz} \\ \mathcal{A}_1^{Mx} & 0 \\ 0 & 0 \\ \mathcal{A}_1^{My} & \mathcal{A}_3^{My} \end{bmatrix} \begin{pmatrix} V_1(t) \\ V_3(t) \end{pmatrix} R(y). \quad (16b)$$

4.3. Linearized governing equations

85 Approximating the trigonometric functions of Eqs. (11)-(12) with their Taylor series expansion, i.e. $\sin \phi \approx \phi$ and $\cos \phi \approx 1$, the CAS lay-up configuration equations can be split into two subsystem, the *Lateral Bending-Extension coupling subsystem* ($u_0 - v_0 - \theta_z$) and the *Twist-Vertical Bending coupling subsystem* ($w_0 - \phi - \theta_x$).

*BE-subsystem (Lateral **B**ending-**E**xtension coupling subsystem).*

$$\delta u_0 : a_{14}v_0'' + a_{44}(u_0'' + \theta_z') - b_1\ddot{u}_0 + p_x + \delta_p \mathcal{A}_2^{Qx} V_2 R'(y) = 0, \quad (17a)$$

$$\delta v_0 : a_{11}v_0'' + a_{14}(u_0'' + \theta_z') - b_1\ddot{v}_0 + p_y + \delta_p \mathcal{A}_2^{Ty} V_2 R'(y) + \delta_p \mathcal{A}_4^{Ty} V_4 R'(y) = 0, \quad (17b)$$

$$\begin{aligned} \delta \theta_z : a_{22}\theta_z'' - a_{14}v_0' + a_{44}(u_0' + \theta_z) - (b_5 + b_{15})\ddot{\theta}_z + m_z + \delta_p \mathcal{A}_3^{Mz} V_3 R'(y) \\ - (\delta_p + \delta_s) \mathcal{A}_2^{Qx} V_2 R(y) = 0. \end{aligned} \quad (17c)$$

The boundary conditions for cantilevered beams are

at $y = 0$:

$$u_0 = v_0 = \theta_z = 0, \quad (18)$$

and at $y = L$:

$$\delta u_0 : a_{14}v'_0 + a_{44}(u'_0 + \theta_z) + \delta_s \mathcal{A}_2^{Qx} V_2 = \bar{Q}_x, \quad (19a)$$

$$\delta v_0 : a_{11}v'_0 + a_{14}(u'_0 + \theta_z) + \delta_s \mathcal{A}_2^{Ty} V_2 + \delta_s \mathcal{A}_4^{Ty} V_4 = \bar{T}_y, \quad (19b)$$

$$\delta \theta_z : a_{22}\theta'_z + \delta_s \mathcal{A}_3^{Mz} V_3 = \bar{M}_z. \quad (19c)$$

TB-subsystem (Twist-Vertical Bending coupling subsystem).

$$\delta w_0 : a_{55}(w''_0 + \theta'_x) - b_1 \ddot{w}_0 + p_z + \delta_p \mathcal{A}_4^{Qz} V_4 R'(y) = 0, \quad (20a)$$

$$\begin{aligned} \delta \phi : a_{37}\theta''_x + a_{77}\phi'' - a_{66}\phi^{(iv)} - (b_4 + b_5)\ddot{\phi} + (b_{10} + b_{18})\phi'' + m_y + b'_w \\ + \delta_p \mathcal{A}_1^{My} V_1 R'(y) + \delta_p \mathcal{A}_3^{My} V_3 R'(y) = 0, \end{aligned} \quad (20b)$$

$$\begin{aligned} \delta \theta_x : a_{33}\theta''_x + a_{37}\phi'' - a_{55}(w'_0 + \theta_x) - (b_4 + b_{14})\ddot{\theta}_x + m_x + \delta_p \mathcal{A}_1^{Mx} V_1 R'(y) \\ - (\delta_p + \delta_s) \mathcal{A}_4^{Qz} V_4 R(y) = 0, \end{aligned} \quad (20c)$$

The boundary conditions, for cantilevered beams are

at $y = 0$:

$$w_0 = \phi = \phi' = \theta_x = 0, \quad (21)$$

and at $y = L$:

$$\delta w_0 : a_{55}(w'_0 + \theta_x) + \delta_s \mathcal{A}_4^{Qz} V_4 = 0, = \bar{Q}_z, \quad (22a)$$

$$\delta \phi : a_{37}\theta'_x + a_{77}\phi' - a_{66}\phi + (b_{10} + b_{18})\phi' + \delta_s \mathcal{A}_1^{My} V_1 + \delta_s \mathcal{A}_3^{My} V_3 = \bar{M}_y, \quad (22b)$$

$$\delta\phi' : a_{66}\phi'' = \bar{B}_w, \quad (22c)$$

$$\delta\theta_x : a_{33}\theta'_x + a_{37}\phi' + \delta_s \mathcal{A}_1^{Mx} V_1 = \bar{M}_x, \quad (22d)$$

90 If the actuator is spread over the entire beam span, the traces are $\delta_p = 0$ and $\delta_s = 1$; otherwise, if the actuator is a single patch, the traces assume the values $\delta_p = 1$ and $\delta_s = 0$. Note that the BE-subsystem and the TB-subsystem are not entirely independent, since they are coupled by the voltage parameters V_3 and V_4 .

95 5. Solution methodology

The Extend Galerkin's Method (EGM) [27, 28] is used to discretize the system. EGM adopts weighting (or shape) functions that need to fulfill only the essential boundary conditions. Natural boundary conditions do not appear explicitly in the functional, and are satisfied in a weak sense. Symmetric mass and stiffness matrices will be obtained for thin-walled beams with CAS lay-ups. From now on, bold fonts will denote vectors or matrices, with regular fonts denoting scalar variables. Thus,

$$\begin{aligned} u_0(y, t) &= \mathbf{\Psi}_u^T(y) \mathbf{q}_u(t), & v_0(y, t) &= \mathbf{\Psi}_v^T(y) \mathbf{q}_v(t), & w_0(y, t) &= \mathbf{\Psi}_w^T(y) \mathbf{q}_w(t), \\ \phi(y, t) &= \mathbf{\Psi}_\phi^T(y) \mathbf{q}_\phi(t), & \theta_x(y, t) &= \mathbf{\Psi}_x^T(y) \mathbf{q}_x(t), & \theta_z(y, t) &= \mathbf{\Psi}_z^T(y) \mathbf{q}_z(t), \end{aligned} \quad (23)$$

where the shape functions $\mathbf{\Psi}_u^T(y)$, $\mathbf{\Psi}_v^T(y)$, \dots , $\mathbf{\Psi}_z^T(y)$ are required to fulfill only the essential boundary conditions.

Equations (17)-(19) and (20)-(22) lead to the following discretized equations of motion,

$$[\mathbf{M}]_{(B,T)} \{\ddot{\mathbf{q}}\}_{(B,T)} + [\mathbf{K}]_{(B,T)} \{\mathbf{q}\}_{(B,T)} + [\mathcal{A}]_{(B,T)} \{\mathbf{V}\}_{(B,T)} = [\mathbf{Q}]_{(B,T)}, \quad (24)$$

where the subscript B , T denote the BE-subsystem and TB-subsystem, respectively, and $\mathbf{q}_B = \{\mathbf{q}_u^T \ \mathbf{q}_v^T \ \mathbf{q}_z^T\}^T$, $\mathbf{q}_T = \{\mathbf{q}_w^T \ \mathbf{q}_\phi^T \ \mathbf{q}_x^T\}^T$, $\mathbf{V}_B = \{V_2 \ V_3 \ V_4\}^T$,

100 $\mathbf{V}_T = \{V_1 \ V_3 \ V_4\}^T$. The expressions for mass matrix $\mathbf{M}_{(B,T)}$, stiffness matrix $\mathbf{K}_{(B,T)}$, actuation matrix $\mathcal{A}_{(B,T)}$ and external excitation vector $\mathbf{Q}_{(B,T)}$ are given in Appendix B.

6. Model validations

The beam simplified model is firstly validated by comparing the vibration
 105 frequency predicted for a composite thin-walled beam with the analytical results of Ref. [29] and the experimental data of Ref. [30]. The geometry and material properties of the cantilever thin-walled box beam of Fig. 1 are specified in Table 1. The results, reported in Table 2, show a better agreement of the present model with experimental data than that of Ref. [29].

Table 1: Details of thin-walled composite box beam for validation [30]

E_{11}	$1.42 \times 10^{11} \text{ N/m}^2$	Density (ρ)	$1.442 \times 10^3 \text{ Kg/m}^3$
$E_{22} = E_{33}$	$9.8 \times 10^9 \text{ N/m}^2$	Width ($2b^a$)	$2.268 \times 10^{-2} \text{ m}$
$G_{12} = G_{13}$	$6.0 \times 10^9 \text{ N/m}^2$	Depth ($2d^a$)	$1.212 \times 10^{-2} \text{ m}$
G_{23}	$4.83 \times 10^9 \text{ N/m}^2$	Number of layers (N_p)	6
$\mu_{12} = \mu_{13}$	0.42	Layer thickness	$1.270 \times 10^{-4} \text{ m}$
μ_{23}	0.50	Length (L)	0.8446 m

^a Inner dimensions of the cross section.

Table 2: Natural frequency (Hz) for $[45]_6$ CAS lay-up configuration

Mode	Exp. [30]	Analytical [29]	Error (%)	Present	Error ^a (%)
1TB	16.67	14.69	-11.9	15.20	-8.8
2TB	96.15	92.02	-4.3	95.09	-1.1
1BE	29.48	25.13	-14.8	26.64	-9.6

^a Relative error, $(\text{Present} - \text{Exp.})/\text{Exp.} \times 100\%$.

110 The piezo-composite actuator model validation is based on the results obtained for a 1/16th scale blade with NACA 0012 airfoil single-cell cross-section [31].

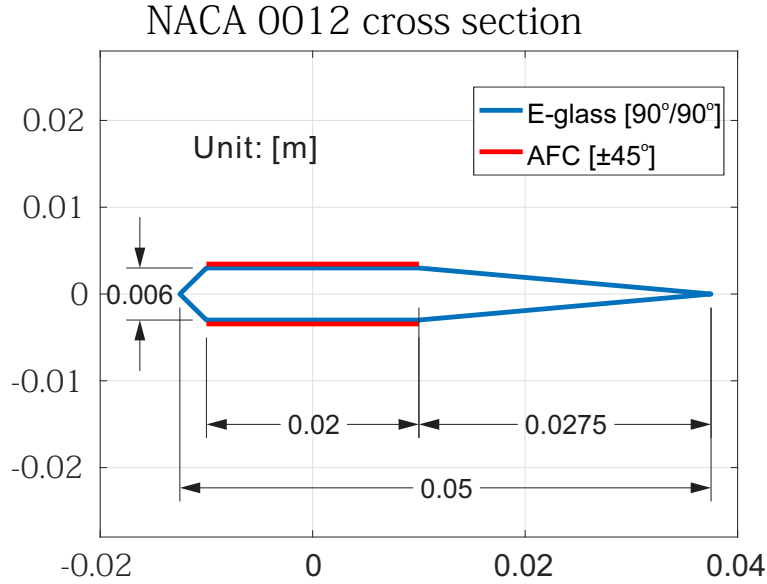


Figure 3: NACA0012 airfoil cross-section.

The cross-section geometry is shown in Fig. 3. The AFC fibers are aligned at $+45^\circ$ and -45° at the blade top and bottom, respectively. The E-glass and AFC material properties are reported in Table 3. Fig. 4 shows the induced tip twist angle as a function of the applied voltage, with a good agreement with Ref. [31].

7. Static study

The material property (Graphite-Epoxy) and geometric specification for the thin-walled box beam of Fig. 1 are shown in Table 4. In order to obtain better actuating performance [32], the piezo-actuators are manufactured by single crystal MFC, whose material property is specified in Table 3. Moreover, the piezo-composite laminate is distributed over the entire cross-section. The lay-up configurations (both for host structure and piezo-actuator) can be found in Table 5.

Table 3: Material properties of E-glass, AFC and single crystal MFC (S-MFC)

	E-Glass [31]	AFC [31]	S-MFC [32]
E_1 (Gpa)	14.8	30.54	6.23
E_2 (Gpa)	13.6	16.11	11.08
G_{12} (Gpa)	1.9	5.5	2.01
μ_{12}	0.19	0.36	0.229
d_{11} ($\times 10^{-12}$ m/V)	N/A	381	1896.5
d_{12} ($\times 10^{-12}$ m/V)	N/A	-160	-838.2
ρ (Kg m $^{-3}$)	1700	4810	5338.3
Thickness ($\times 10^{-4}$ m)	2.032	1.689	17
Electrode spacing ($\times 10^{-3}$ m)	N/A	1.143	1.7

Table 4: Material property and geometric specification of the host structure [33, p. 131]

E_{11}	206.8×10^9 N/m 2	Width ($2b^a$)	0.254 m
$E_{22} = E_{33}$	5.17×10^9 N/m 2	Depth ($2d^a$)	0.0681 m
$G_{12} = G_{13}$	2.55×10^9 N/m 2	Wall thickness (h)	0.0102 m
G_{23}	3.10×10^9 N/m 2	Number of layers (N_p)	6
$\mu_{12} = \mu_{13} = \mu_{23}$	0.25	Layer thickness	0.0017 m
ρ	1.528×10^3 Kg/m 3	Length (L)	2.032 m

^a The length is measured on the mid-line contour.

125 7.1. Piezo-actuator coefficients study

The non-zero CAS configuration piezo-actuator coefficients of Eq.(16) are depicted in Figs. 5 and 6 as a function of the piezo-actuator ply-angle θ_p . Two distinct trends emerge from the results of Figs. 5 and 6.

The first trend characterizes the bending coefficients (\mathcal{A}_1^{Mx} , \mathcal{A}_3^{Mz}) and the
130 extension coefficients (\mathcal{A}_2^{Ty} , \mathcal{A}_4^{Ty}). The coefficients increase from $\theta_p = 0^\circ$ to $\theta_p = 90^\circ$, then decrease until $\theta_p = 180^\circ$. Their values equal zero when $\theta_p \approx 40^\circ$ and $\approx 140^\circ$. Note that, because of the reverse definition of θ_x (see Fig. 1), coefficients \mathcal{A}_1^{Mx} and \mathcal{A}_3^{Mz} present the exactly opposite trends.

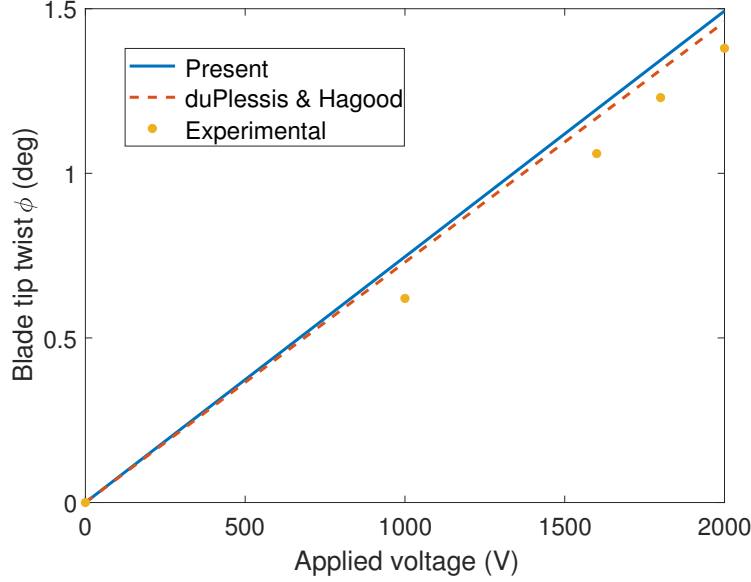


Figure 4: Tip deflection

The second trend characterizes the transverse shear coefficients (\mathcal{A}_2^{Qx} , \mathcal{A}_4^{Qz}) and the twist coefficients (\mathcal{A}_1^{My} , \mathcal{A}_3^{My}). The previous groups of coefficients have a symmetric dependence centered around $\theta_p = 90^\circ$. These coefficients, instead, show an anti-symmetric trend around $\theta_p = 90^\circ$. They are equal to zero when $\theta_p = 0^\circ$, 90° , 180° , with the maximum absolute values reached for $\theta_p \approx 42^\circ$ and $\theta_p \approx 138^\circ$.

Table 5: Lay-up configurations for beam with CAS lay-up [unit:deg].

Material	Layer	Flanges		Webs	
		Top	Bottom	Left	Right
Piezo-actuator	CAS (7) ^a	$[\theta_p]$	$[\theta_p]$	$[\theta_p]$	$[\theta_p]$
Host structure	CAS (1-6)	$[\theta_h]_6$	$[\theta_h]_6$	$[\theta_h / -\theta_h]_3$	$[\theta_h / -\theta_h]_3$

^a The piezo-actuator is positioned of the outer side of the laminate.

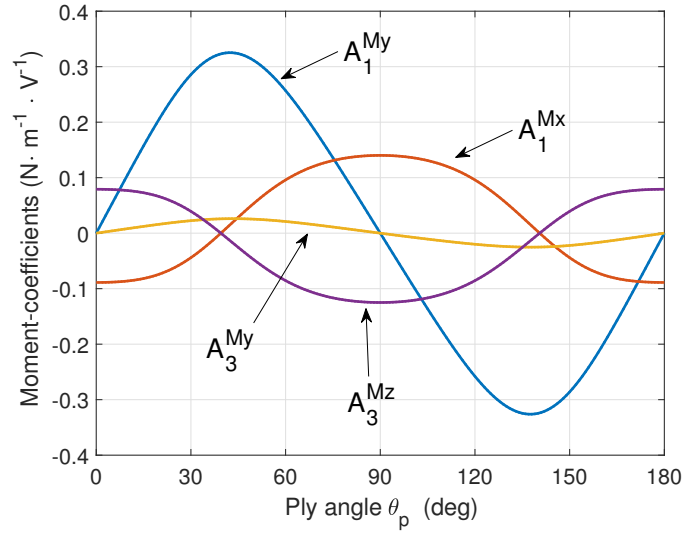


Figure 5: Actuating moment coefficients with single crystal MFC as a function of the ply-angle θ_p in CAS lay-up configuration.

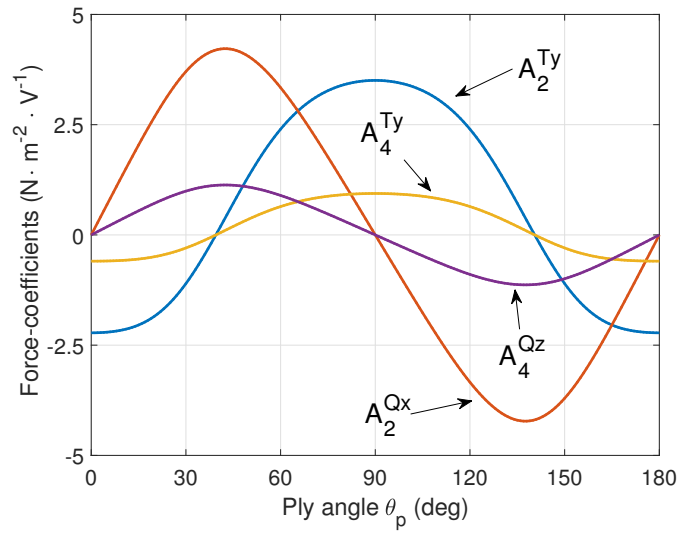


Figure 6: Actuating force coefficients with single crystal MFC as a function of the ply-angle θ_p in CAS lay-up configuration.

140 *7.2. Actuation performance study*

In this subsection, the relationship between actuation performance and voltage parameters (V_1, V_2, V_3, V_4) is specifically discussed.

7.2.1. TB-subsystem

The equations governing the TB-subsystem in Eqs. (20), have the voltage
 145 vector $\mathbf{V}_T = [V_1, V_3, V_4]^T$ as forcing parameters. Specifically, the voltage parameter V_1 influences both twist and bending, while V_3 and V_4 work for twist and transverse shear, respectively. Note that the elastic coupling of the structure has a significant effect on the actuation performance. The twist-bending elastic coupling in Eq. (14b) is related to the stiffness coefficient a_{37} . Two typical
 150 host structure ply-angles, viz., $\theta_h = 15^\circ$ and $\theta_h = 75^\circ$, are considered here. The corresponding values for a_{37} were computed in Ref. [26], i.e., a_{37} equals $-4.05 \times 10^3 \text{ N.m}^2$ and $3.92 \times 10^5 \text{ N.m}^2$, respectively. Thus, the elastic coupling can be ignored for $\theta_h = 15^\circ$, while it is significant for $\theta_h = 75^\circ$.

Figures 7 and 8 depict the tip deflections obtained from $V_1 = 1000 \text{ V}$ (black curve), $V_3 = 1000 \text{ V}$ (red curve) and $V_4 = 1000 \text{ V}$ (green curve) for weak and strong elastic coupling cases, respectively. The non-dimensional quantities are defined as

$$\hat{u}_0 = \frac{u_0}{2b}, \quad \hat{v}_0 = \frac{v_0}{L}, \quad \hat{w}_0 = \frac{w_0}{2b}, \quad \hat{\phi} = \phi, \quad \hat{\theta}_x = \theta_x, \quad \hat{\theta}_z = \theta_z. \quad (25)$$

155 It can be seen that the voltage parameter V_4 , which is related to transverse-shear-actuation can be ignored in both cases. In addition, the voltage parameter V_1 dominates the TB-subsystem actuation performance. Note that, for strong elastic coupling case in Fig. 8, twist-actuation shows better performance on bending deflection than direct bending-actuation.

160 *7.2.2. BE-subsystem*

According to the governing equations (17) of the BE-subsystem, voltage V_2 is related to both extension and transverse shear actuation, while V_3 and V_4 are

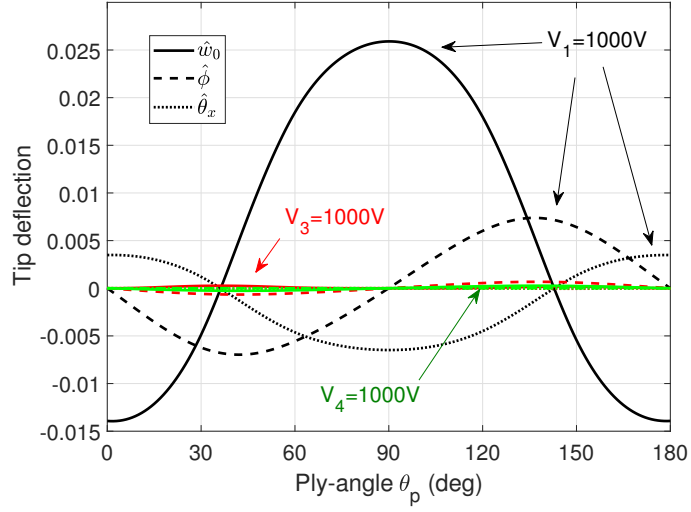


Figure 7: Beam tip deflections of the TB-subsystem ($\theta_h = 15^\circ$) as a function of the piezo-actuator ply-angle θ_p .

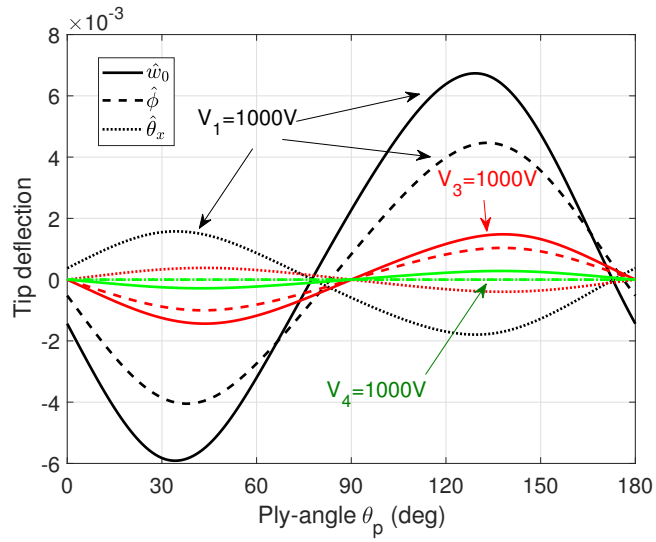


Figure 8: Beam tip deflections of the TB-subsystem ($\theta_h = 75^\circ$) as a function of the piezo-actuator ply-angle θ_p .

related to bending and extension actuation, respectively. The results obtained for two typical host structure cases, $\theta_h = 15^\circ$ and $\theta_h = 75^\circ$, are reported in Figs. 9 and 10.

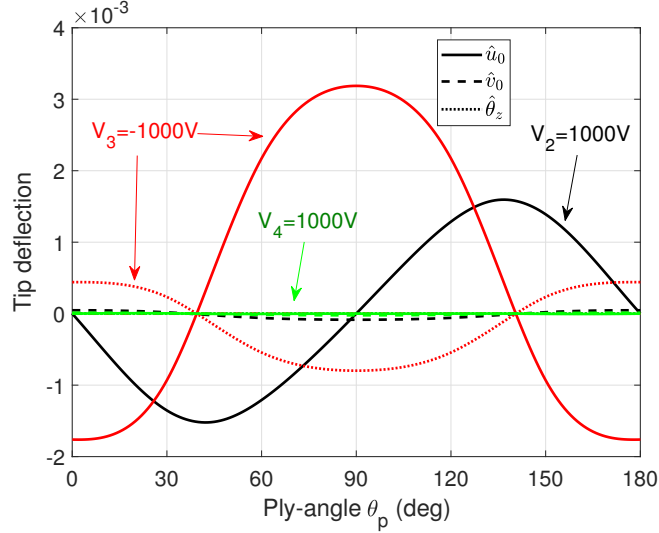


Figure 9: Beam tip deflections of BE-subsystem ($\theta_h = 15^\circ$) as a function of the piezo-actuator ply-angle θ_p .

165

The beam extension stiffness coefficient a_{11} is much higher than the other terms. Thus, the extension actuation induced by voltage parameter V_4 can be ignored, see both Figs. 9 and 10. The voltage V_2 has a significant effect on actuation performance for both cases: the transverse-shear-actuation, weak in the TB-subsystem, is much stronger in the BE-subsystem. One reason for this is that the size of the flange-actuator-pair is almost four times than that of the web-actuator-pair. In addition, the direct bending actuation induced by voltage V_3 (red line) in the $\theta_h = 75^\circ$ case in Fig. 10 is much weaker than that in the $\theta_h = 15^\circ$ case in Fig. 9.

170

175 7.2.3. Conclusion

In a nutshell, the TB-subsystem is dominated by V_1 for the weak elastic coupling case (see Fig. 7), while the BE-subsystem is dominated by V_2 when

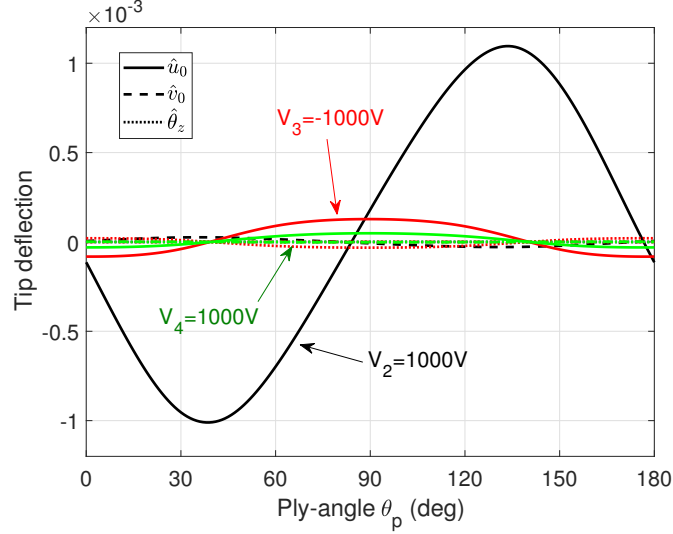


Figure 10: Beam tip deflections of BE-subsystem ($\theta_h = 75^\circ$) as a function of the piezo-actuator ply-angle θ_p .

the elastic coupling effect is strong (see Fig. 10). As a result, although the TB-subsystem and the BE-system are actually coupled by V_3 and V_4 , it is nonetheless reasonable to treat these two subsystems as independent.

8. Dynamic control: negative velocity feedback control

8.1. Governing equations including negative velocity feedback control

A negative velocity feedback control is considered here. Since we are interested in the aeroelastic control of an aircraft wing we choose to focus this investigation into the torsion/bending (TB) subsystem. If we assume the sensor can offer the velocity information at $y = Y_s$, then actuating voltage vector \mathbf{V}_T for the negative velocity feedback control can be computed

$$\mathbf{V}_T = \begin{Bmatrix} V_1 \\ V_3 \\ V_4 \end{Bmatrix} = \begin{Bmatrix} -k_1[\alpha_1^k \dot{\phi}(Y_s, t) + \beta_1^k \dot{\theta}_x(Y_s, t)] \\ -k_3 \dot{\phi}(y, t) \\ -k_4[\alpha_4^k \dot{w}_0(Y_s, t) + \beta_4^k \dot{\theta}_x(Y_s, t)] \end{Bmatrix} = \mathbf{P}(Y_s) \dot{\mathbf{q}}_T(t), \quad (26)$$

where, k_i ($i = 1, 3, 4$) are the feedback control gains, α_i^k and β_i^k are weighting coefficients of the control gains, and matrix \mathbf{P} is defined in Appendix B. As a result, the closed-loop discretized system Eq. (24) becomes

$$\mathbf{M}_T \ddot{\mathbf{q}}_T(t) + \mathcal{A}_T \mathbf{P} \dot{\mathbf{q}}_T(t) + \mathbf{K}_T \mathbf{q}_T(t) = \mathbf{Q}_T(t). \quad (27)$$

8.2. Control gain weighting coefficients discussion

The first step in designing the controller is to choose suitable control weighting coefficients. Since the flapping and twisting motions usually have a significant phase difference, we can simplify the control system by considering only two cases for the voltage parameter V_1 , i.e., the bending control ($\alpha_1^k = 0$, $\beta_1^k = -1$) and the twist control ($\alpha_1^k = 1$, $\beta_1^k = 0$). Furthermore, as evidenced by the static study, the shear force induced by V_4 is immaterial in the TB-subsystem. As a result, the velocity feedback Eq. (26) can be simplified to a combination of these two cases: the Bending Control Methodology,

$$\mathbf{V}_T = \begin{Bmatrix} V_1 \\ V_3 \end{Bmatrix} = \begin{Bmatrix} k_1 \dot{\theta}_x \\ -k_3 \dot{\phi} \end{Bmatrix} \quad (28)$$

and the Twist Control Methodology

$$\mathbf{V}_T = \begin{Bmatrix} V_1 \\ V_3 \end{Bmatrix} = \begin{Bmatrix} -k_1 \dot{\phi} \\ -k_3 \dot{\phi} \end{Bmatrix} \quad (29)$$

The static study in Section 7.2.1 evidenced a significant effect of the twist-
185 bending elastic coupling on the actuation performance. Thus, the weak and strong elastic coupling cases are separately investigated here. Bending control is considered first because twist control has a weak bending authority for the weak elastic coupling case. Fig. 11 depicts the damping ratios obtained for the first four modes of the weak elastic coupling case $\theta_h = 15^\circ$. The figure allows to
190 easily identify the positive damping area $90^\circ \leq \theta_p \leq 138^\circ$. The first four modes are denoted as Flap1, Flap2, Twist1 and Flap3, respectively. Since the twist-bending coupling can be ignored in the first four modes, the damping ratios of the flapping and the twist modes follow the trend of coefficients \mathcal{A}_1^{Mx} and \mathcal{A}_3^{My} variation in Fig. 5, respectively.

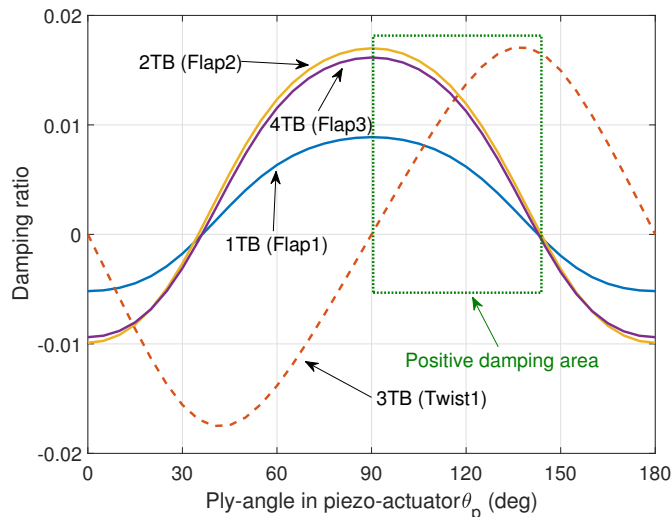


Figure 11: Damping ratios as a function of piezo-composite ply-angle θ_p ; bending control methodology, $k_i = 100$, $\theta_h = 15^\circ$.

195 Considering the strong twist-bending elastic coupling case of $\theta_h = 75^\circ$, the results obtained with the bending control methodology and the twist control methodology are shown in Figs. 12 and 13, respectively. Note that, due to the strong elastic coupling, there will be no pure bending mode or twist mode for the TB-subsystem. The twist control methodology is more efficient, especially for the third mode (3TB), whose modal shape is dominated by the twist component.
 200 This is because the negative twist damping will be induced by direct bending actuation via twist-bending elastic coupling, see Fig. 12.

In a nutshell, the optimal control strategy for the $\theta_h = 15^\circ$ case is the bending control methodology with $\theta_p \approx 120^\circ$, while for the $\theta_h = 75^\circ$ case is the
 205 twist control methodology with $\theta_p \approx 135^\circ$.

8.3. Optimized by tailoring

It is clear that the twist-bending elastic coupling has a significant effect on control efficiency. Thus, in order to optimize the control performance by host structure tailoring, the effect of the ply-angle θ_h at the vibration control

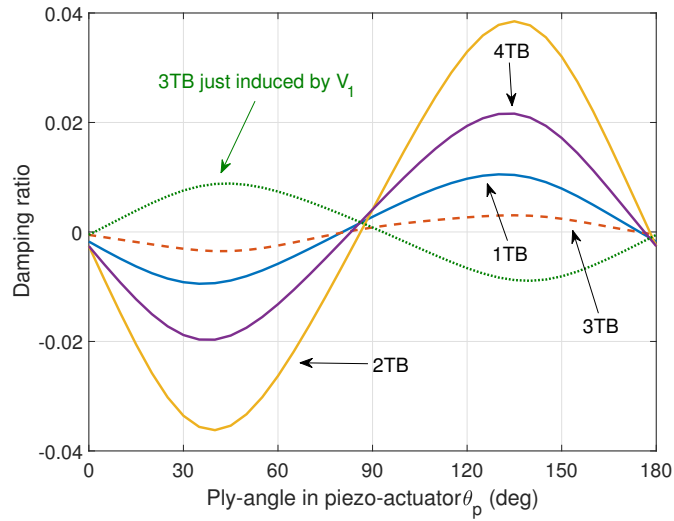


Figure 12: Damping ratios as a function of the piezo-composite ply-angle θ_p ; bending control methodology, $k_i = 100$, $\theta_h = 75^\circ$.

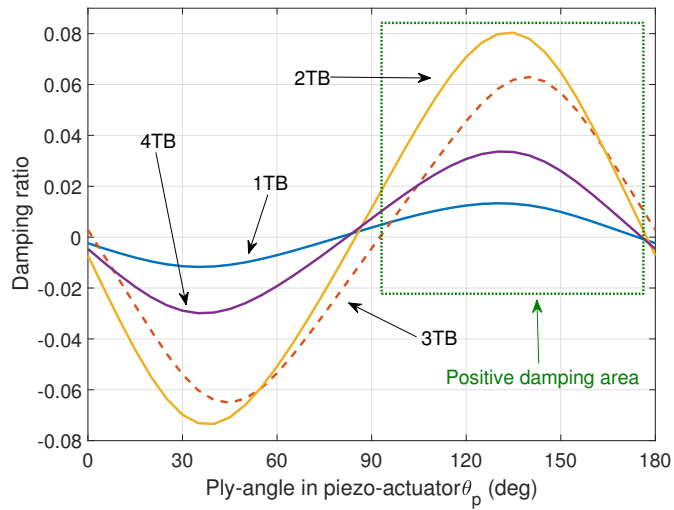


Figure 13: Damping ratios as a function of piezo-composite ply-angle θ_p ; twist control methodology, $k_i = 100$, $\theta_h = 75^\circ$.

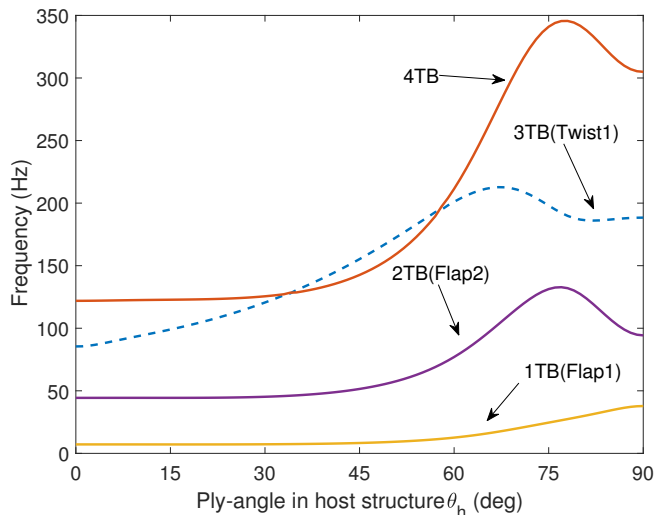


Figure 14: First four modes frequencies as a function of host structure ply-angle θ_h ; $\theta_p = 120^\circ$ and $k_i = 100$.

210 authority is investigated.

Figure 14 depicts the frequencies of the first four modes as a function of angle θ_h . A typical *mode cross* phenomenon between the third and fourth modes can be found in Fig. 14. In order to avoid misunderstanding in the following study, we denote 3TB and 4TB the 4th and 3rd modes in the mode crossed range
 215 $33^\circ < \theta_h < 60^\circ$, respectively. The frequency of mode 1TB increases from $\theta_h = 0^\circ$ to $\theta_h = 90^\circ$; modes 2TB and 4TB reach their maximum frequency for $\theta_h \approx 80^\circ$.

In order to compare the bending and twist control methodologies, $\theta_p = 120^\circ$ in piezo-actuator is adopted here, since this angle allows to achieve compar-
 220 able bending moment and twist authorities. The damping ratios obtained with the bending and the twist control methodology are shown in Figs. 15 and 16, respectively. A sudden change around the mode cross points $\theta_h \approx 33^\circ$ and $\theta_h \approx 58^\circ$ can be found in Figs. 15 and 16. Especially near the point $\theta_h \approx 58^\circ$ in Fig. 15, a jump phenomenon is observed. This is because near this point, not
 225 only the eigen-frequencies of the 3TB and 4TB modes are almost the same, but

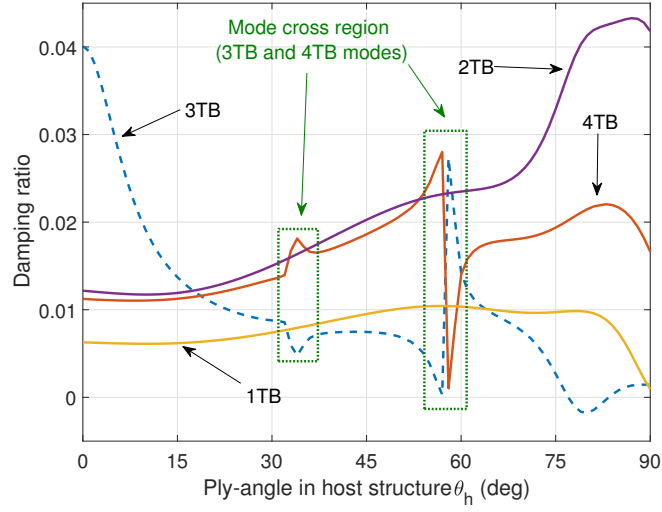


Figure 15: Damping ratio as a function of the host structure ply-angle θ_h , bending control methodology; $\theta_p = 120^\circ$ and $k_i = 100$.

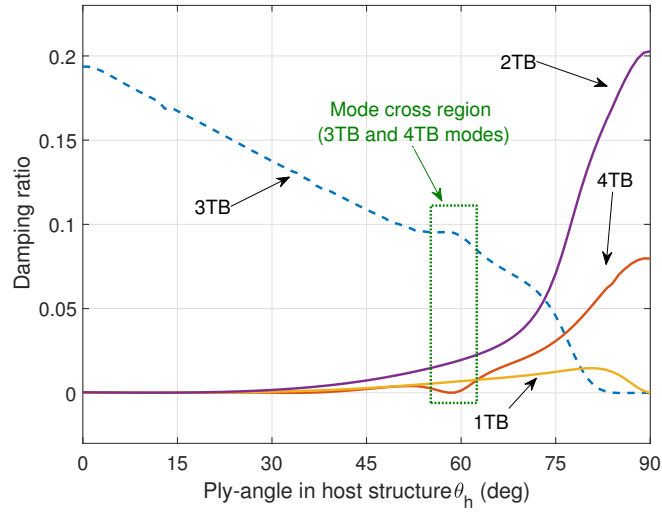


Figure 16: Damping ratio as a function of host structure ply-angle θ_h ; twist control methodology, $\theta_p = 120^\circ$ and $k_i = 100$.

their mode shapes are similar as well. Outside of the mode cross regions, the damping ratios for both control methodologies increase for the 1TB, 2TB and 4TB modes, and decreases for the 3TB mode. Furthermore, for bending control methodology of Fig. 15, mode 3TB has a negative damping above $\theta_h \approx 80^\circ$, and the damping ratios of modes 1TB, 2TB and 3TB significantly decrease near $\theta_h = 90^\circ$.

The absolute value of the first mode (1TB) eigenvalue real part is plotted as a function of θ_h in Fig. 17. The corresponding curves for the 2TB, 3TB and 4TB modes are reported in Fig. 18. The plots of Figs. 17 and 18 can be splitted into two different regions, i.e. Area 1 for $0 < \theta_h < 45^\circ$ and Area 2 for $69^\circ < \theta_h < 87^\circ$; these regions are characterized by weak and strong twist-bending elastic coupling, respectively. In Area 1, the twist control methodology (red lines) has almost no flapping damping; thus, the bending control methodology (black lines) should be chosen. Within Area 2, instead, the flapping damping induced by the elastic coupling allows to achieve a damping that is higher than that of the direct flapping control; thus, the twist control methodology would be a better choice here.

8.4. *Vibration control under an impulsive load*

An impulsive load with coefficients $p_z = m_y = 1$, and $m_x = 0$ in Eqs. (20) is applied to the $\theta_h = 75^\circ$ structure. Figs. 19 and 20 depict the time responses of the tip flapping displacement $\hat{w}_0(L, t)$ and twist rotation $\hat{\phi}(L, t)$, respectively. Piezo-actuator $\theta_p = 90^\circ$ with bending control methodology, that was chosen in Refs. [14, 15, 24], is compared with the piezo-actuator $\theta_p = 135^\circ$ with twist control methodology. From the results of Figs. 19 and 20, it can be seen that the twist control shows a significant advantage both for the flapping and twisting motions.

8.5. *The influence of position of piezo-actuator*

Investigating the effect of size and position of piezo-actuators allows to strike a balance between their cost and efficiency. As reported by Librescu

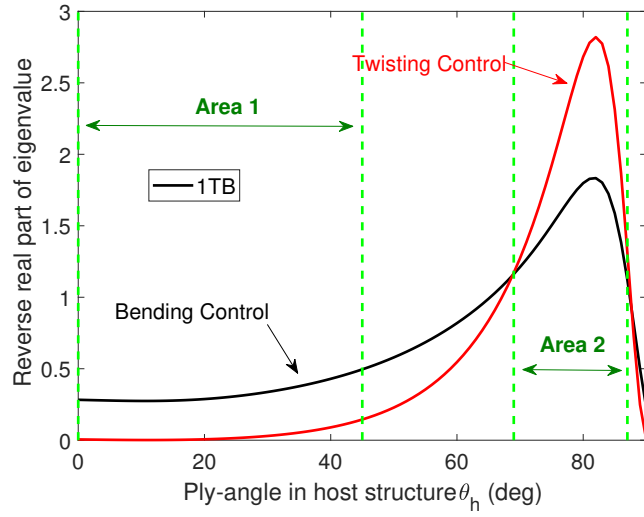


Figure 17: Absolute value of the real part of 1TB eigenvalue as a function of the host structure ply-angle θ_h ; $\theta_p = 120^\circ$, $k_i = 100$.

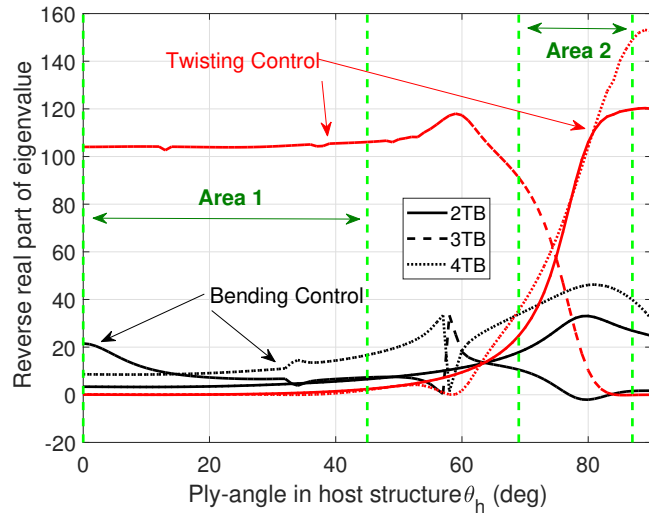


Figure 18: Absolute value of the real part of 2TB, 3TB and 4TB eigenvalues as a function of the host structure ply-angle θ_h ; $\theta_p = 120^\circ$, $k_i = 100$.

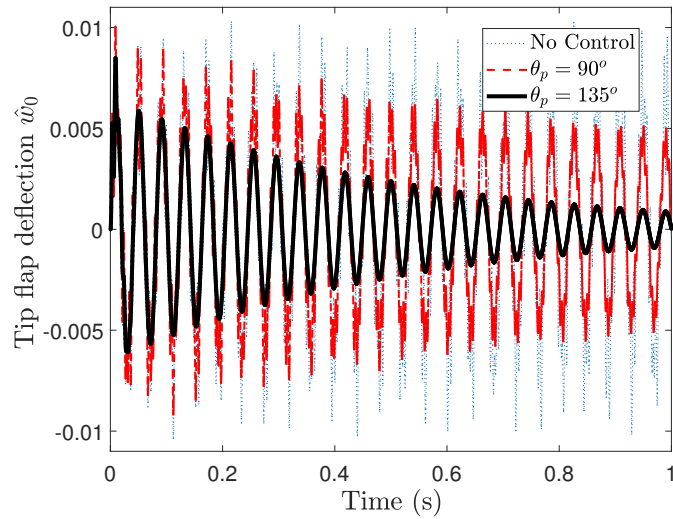


Figure 19: Tip flapping displacement \hat{w}_0 in TB-subsystem ($\theta_h = 75^\circ$) subject to an impulse load; $k_i = 100$.

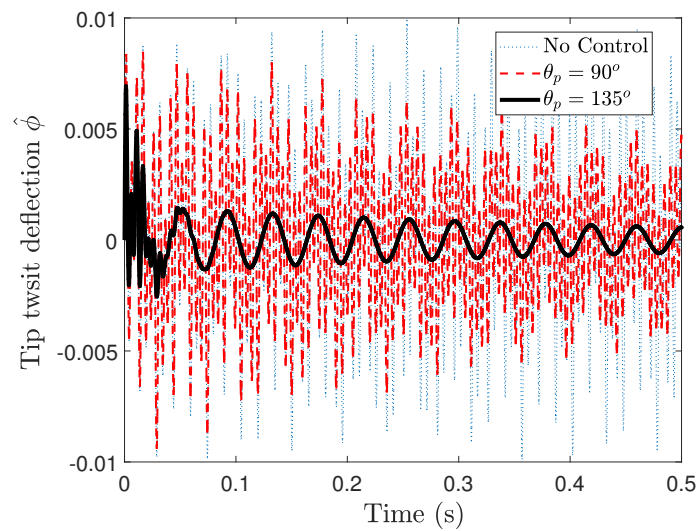


Figure 20: Tip twist rotation $\hat{\phi}$ in TB-subsystem ($\theta_h = 75^\circ$) subject to an impulse load; $k_i = 100$.

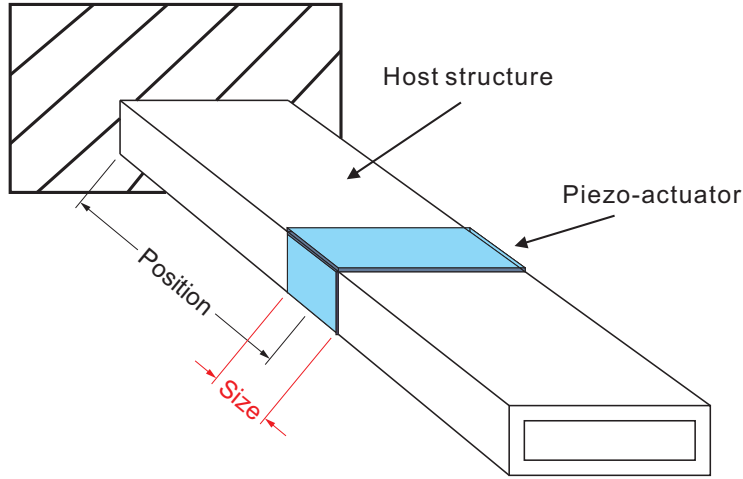


Figure 21: Position and size of the piezo-actuator.

255 et al [20, 21], twist-bending elastic coupling is beneficial for the aeroelastic re-
 sponse behavior. Thus the piezo-actuator $\theta_p = 135^\circ$ with twist control method-
 ology and strong elastic coupling host structure $\theta_h = 75^\circ$ is considered here.
 The size of the piezo-actuator is first fixed at 10% of the beam span, and the
 sensors are applied at the outer end of the piezo-actuator, see Fig. 21. The
 260 resulting first four modes damping ratios are depicted in Fig. 22 as a function
 of the piezo-actuator position. When the piezo is positioned between 48% and
 67% of the wing span, the 4TB mode damping is negative. A good compromise
 is achieved at 40% of the span. However, for a large size piezo-actuator, e.g.,
 70% length of span see Fig. 23, the damping ratios of the first four modes are
 265 all positive. In a nutshell, the optimized position for piezo-actuator is around
 central point of the span.

9. Summary and conclusions

A geometrical nonlinear fiber-reinforced composite thin-walled beam theory
 incorporating piezo-composite actuators is developed and used to model a smart
 270 aircraft wing. A circumferential asymmetric stiffness (CAS) lay-up configura-
 tion is adopted in order to split the linear system into two subsystems, viz.,

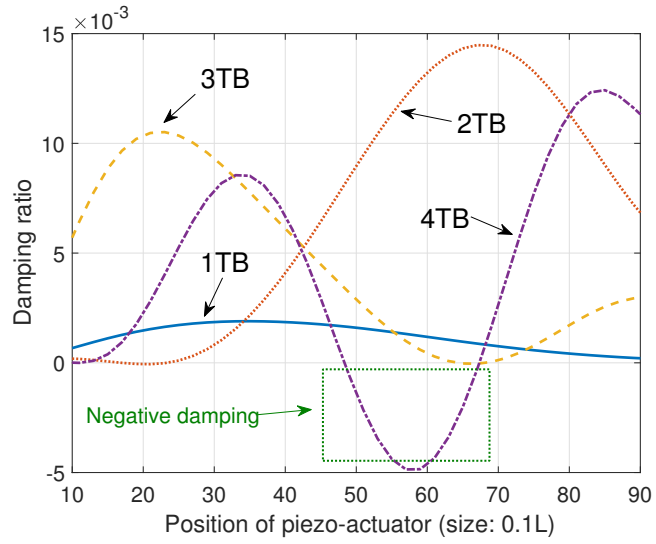


Figure 22: Damping ratios as a function of the piezo-actuator position; $\theta_h = 75^\circ$, $\theta_p = 135^\circ$, $k_i = 100$.

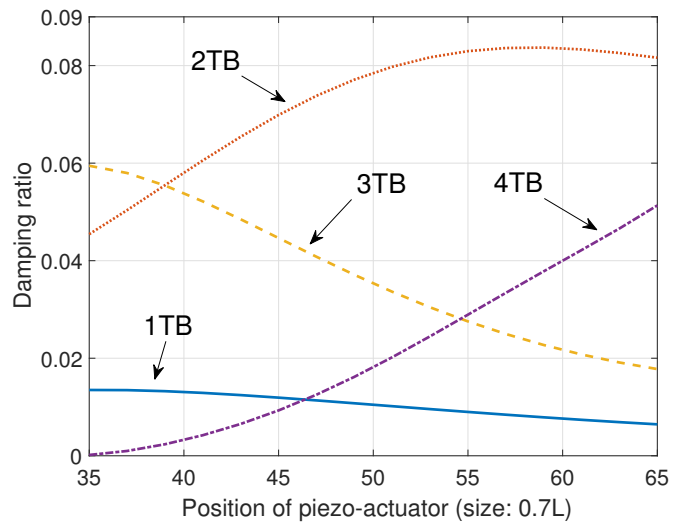


Figure 23: Damping ratios as a function of the piezo-actuator position; $\theta_h = 75^\circ$, $\theta_p = 135^\circ$, $k_i = 100$.

the lateral bending-extension coupled subsystem and the twist-vertical bending coupled subsystem. A simple negative velocity feedback control algorithm is proposed, and used to assess how the piezo-actuator and the fiber-reinforced host structure elastic tailoring influence the vibration suppression control. The main conclusions are that

1. the twist bending elastic coupling of the host structure is beneficial for active damping performance;
2. the transverse shear force actuation is immaterial in TB-subsystem, and the inducing voltage V_4 can be ignored in dynamical control;
3. for the strong twist elastic coupling case, the twist control presents a better flapping control efficiency than the direct bending control;
4. optimizing the size and position of the piezo-actuator can improve the damping control authority and reduce the overall cost of the structure.

285 **Appendix A. The piezo-actuator coefficients \mathcal{A}_i^F**

The subscript $i = 1, 2, 3, 4$ of piezo-actuator coefficients \mathcal{A}_i^F denote the operation

$$\mathcal{A}_1^F = \int_T \mathcal{A}_T^F ds - \int_B \mathcal{A}_B^F ds, \quad \mathcal{A}_2^F = \int_T \mathcal{A}_T^F ds + \int_B \mathcal{A}_B^F ds, \quad (\text{A.1a})$$

$$\mathcal{A}_3^F = \int_L \mathcal{A}_L^F ds - \int_R \mathcal{A}_R^F ds, \quad \mathcal{A}_4^F = \int_L \mathcal{A}_L^F ds + \int_R \mathcal{A}_R^F ds, \quad (\text{A.1b})$$

where T, B, L, R denotes top, bottom, left and right wall, respectively. The definitions of \mathcal{A}^F are given as

$$\mathcal{A}^{Ty} = \sum_{k=1}^{N_p} \left(e_{yy} - \frac{A_{12}}{A_{11}} e_{ss} \right) \frac{[n^{(k)} - n^{(k-1)}]}{\hat{h}} R_{(k)}(s), \quad (\text{A.2a})$$

$$\begin{aligned} \mathcal{A}^{Mz} = & \sum_{k=1}^{N_p} \left\{ x \left(e_{yy} - \frac{A_{12}}{A_{11}} e_{ss} \right) \frac{[n^{(k)} - n^{(k-1)}]}{\hat{h}} R_{(k)}(s) \right. \\ & \left. - \frac{dz}{ds} \left[\frac{1}{2} e_{yy} [n^{(k)} + n^{(k-1)}] - \frac{B_{12}}{A_{11}} e_{ss} \right] \frac{[n^{(k)} - n^{(k-1)}]}{\hat{h}} R_{(k)}(s) \right\}, \end{aligned} \quad (\text{A.2b})$$

$$\begin{aligned} \mathcal{A}^{Mx} = & \sum_{k=1}^{N_p} \left\{ z \left(e_{yy} - \frac{A_{12}}{A_{11}} e_{ss} \right) \frac{[n^{(k)} - n^{(k-1)}]}{\hat{h}} R_{(k)}(s) \right. \\ & \left. + \frac{dx}{ds} \left[\frac{1}{2} e_{yy} [n^{(k)} + n^{(k-1)}] - \frac{B_{12}}{A_{11}} e_{ss} \right] \frac{[n^{(k)} - n^{(k-1)}]}{\hat{h}} R_{(k)}(s) \right\}, \end{aligned} \quad (\text{A.2c})$$

$$\mathcal{A}^{Qx} = \sum_{k=1}^{N_p} \frac{dx}{ds} \left(e_{sy} - \frac{A_{16}}{A_{11}} e_{ss} \right) \frac{[n^{(k)} - n^{(k-1)}]}{\hat{h}} R_{(k)}(s), \quad (\text{A.2d})$$

$$\mathcal{A}^{Qz} = \sum_{k=1}^{N_p} \frac{dz}{ds} \left(e_{sy} - \frac{A_{16}}{A_{11}} e_{ss} \right) \frac{[n^{(k)} - n^{(k-1)}]}{\hat{h}} R_{(k)}(s), \quad (\text{A.2e})$$

$$\begin{aligned} \mathcal{A}^{Bw} = & - \sum_{k=1}^{N_p} \left\{ F_w \left(e_{yy} - \frac{A_{12}}{A_{11}} e_{ss} \right) \frac{[n^{(k)} - n^{(k-1)}]}{\hat{h}} R_{(k)}(s) \right. \\ & \left. + a(s) \left[\frac{1}{2} e_{yy} [n^{(k)} + n^{(k-1)}] - \frac{B_{12}}{A_{11}} e_{ss} \right] \frac{[n^{(k)} - n^{(k-1)}]}{\hat{h}} R_{(k)}(s) \right\}, \end{aligned} \quad (\text{A.2f})$$

$$\begin{aligned} \mathcal{A}^{My} &= \sum_{k=1}^{N_p} \left\{ \psi(s) \left(e_{sy} - \frac{A_{16}}{A_{11}} e_{ss} \right) \frac{[n^{(k)} - n^{(k-1)}]}{\hat{h}} R_{(k)}(s) \right. \\ &\quad \left. + 2 \left[\frac{1}{2} e_{sy} [n^{(k)} + n^{(k-1)}] - \frac{B_{16}}{A_{11}} e_{ss} \right] \frac{[n^{(k)} - n^{(k-1)}]}{\hat{h}} R_{(k)}(s) \right\}, \end{aligned} \quad (\text{A.2g})$$

$$\begin{aligned} \mathcal{A}^{\Gamma t} &= \sum_{k=1}^{N_p} \left\{ (x^2 + z^2) \left(e_{yy} - \frac{A_{12}}{A_{11}} e_{ss} \right) \frac{[n^{(k)} - n^{(k-1)}]}{\hat{h}} R_{(k)}(s) \right. \\ &\quad \left. + 2r_n \left[\frac{1}{2} e_{yy} [n^{(k)} + n^{(k-1)}] - \frac{B_{12}}{A_{11}} e_{ss} \right] \frac{[n^{(k)} - n^{(k-1)}]}{\hat{h}} R_{(k)}(s) \right\}. \end{aligned} \quad (\text{A.2h})$$

Appendix B. Matrix via the Extended Galerkin's Method

Mass matrix.

$$\mathbf{M}_B = \int_0^L \begin{bmatrix} b_1 \Psi_u \Psi_u^T & 0 & 0 \\ & b_1 \Psi_v \Psi_v^T & 0 \\ \text{Symm} & & (b_5 + b_{15}) \Psi_z \Psi_z^T \end{bmatrix} dy, \quad (\text{B.1})$$

$$\mathbf{M} = \int_0^L \begin{bmatrix} b_1 \Psi_w \Psi_w^T & 0 & 0 \\ & (b_4 + b_5) \Psi_\phi \Psi_\phi^T + (b_{10} + b_{18}) \Psi'_\phi \Psi'^T_\phi & 0 \\ \text{Symm} & & (b_4 + b_{14}) \Psi_x \Psi_x^T \end{bmatrix} dy. \quad (\text{B.2})$$

Stiffness matrix.

$$\mathbf{K}_B = \int_0^L \begin{bmatrix} a_{44} \Psi'_u \Psi'^T_u & a_{14} \Psi'_u \Psi'_v{}^T & a_{44} \Psi'_u \Psi'_z{}^T \\ & a_{11} \Psi'_v \Psi'_v{}^T & a_{14} \Psi'_v \Psi'_z{}^T \\ \text{Symm} & & a_{22} \Psi'_z \Psi'_z{}^T + a_{44} \Psi_z \Psi_z{}^T \end{bmatrix} dy, \quad (\text{B.3})$$

$$\mathbf{K}_T = \int_0^L \begin{bmatrix} a_{55} \Psi'_w \Psi'_w{}^T & 0 & a_{55} \Psi'_w \Psi'_x{}^T \\ & a_{77} \Psi'_\phi \Psi'_\phi{}^T + a_{66} \Psi''_\phi \Psi''_\phi{}^T & a_{37} \Psi'_\phi \Psi'_x{}^T \\ \text{Symm} & & a_{33} \Psi'_x \Psi'_x{}^T + a_{55} \Psi_x \Psi_x{}^T \end{bmatrix} dy. \quad (\text{B.4})$$

Piezo-actuator Matrix.

$$\mathcal{A}_B = \int_0^L \begin{bmatrix} \mathcal{A}_2^{Qx} \Psi_u R'(y) & 0 & 0 \\ \mathcal{A}_2^{Ty} \Psi_v R'(y) & 0 & \mathcal{A}_4^{Ty} \Psi_v R'(y) \\ -\mathcal{A}_2^{Qx} \Psi_z R(y) & \mathcal{A}_3^{Qz} \Psi_z R'(y) & 0 \end{bmatrix} dy, \quad (\text{B.5})$$

$$\mathcal{A}_T = \int_0^L \begin{bmatrix} 0 & 0 & \mathcal{A}_4^{Qz} \Psi_w R'(y) \\ \mathcal{A}_1^{My} \Psi_\phi R'(y) & \mathcal{A}_3^{My} \Psi_\phi R'(y) & 0 \\ \mathcal{A}_1^{Mx} \Psi_x R'(y) & 0 & -\mathcal{A}_4^{Qz} \Psi_x R(y) \end{bmatrix} dy, \quad (\text{B.6})$$

External forces vector.

$$\mathbf{Q}_B = \left\{ \begin{array}{l} \int_0^L p_x \Psi_u dy + \bar{Q}_x \Psi_u(L) \\ \int_0^L p_y \Psi_v dy + \bar{T}_y \Psi_v(L) \\ \int_0^L m_z \Psi_z dy + \bar{M}_z \Psi_z(L) \end{array} \right\}, \quad (\text{B.7})$$

$$\mathbf{Q}_T = \left\{ \begin{array}{l} \int_0^L p_z \Psi_w dy + \bar{Q}_z \Psi_w(L) \\ \int_0^L (m_y + b'_w) \Psi_\phi dy + [\bar{M}_y \Psi_\phi(L) + \bar{B}_w \Psi'_\phi(L)] \\ \int_0^L m_x \Psi_x dy + \bar{M}_x \Psi_x(L) \end{array} \right\}. \quad (\text{B.8})$$

Control matrix \mathbf{P} in Eq. (26).

$$\mathbf{P} = \begin{bmatrix} \mathbf{0} & -k_1 \alpha_1^k \Psi_\phi^T(Y_s) & -k_1 \beta_1^k \Psi_x^T(Y_s) \\ \mathbf{0} & -k_3 \Psi_\phi^T(Y_s) & \mathbf{0} \\ -k_4 \alpha_4^k \frac{\Psi_w(Y_s)^T}{2b} & \mathbf{0} & -k_4 \beta_4^k \Psi_x^T(Y_s) \end{bmatrix} \quad (\text{B.9})$$

References

- [1] W. Yu, D. Hodges, J. Ho, Variational asymptotic beam sectional analysis-an updated version, *Int. J. Eng. Sci.* 59 (2012) 40–64.
- 290 [2] S. Ibrahim, E. Carrera, M. Petrolo, E. Zappino, Buckling of composite thin walled beams by refined theory, *Compos. Struct.* 94 (2012) 563–570.
- [3] V. Cortinez, M. Piovan, Vibration and buckling of composite thin-walled beams with shear deformability, *J. Sound Vib.* 258 (2002) 701–723.
- [4] T. P. Vo, J. Lee, Flexural-torsional behavior of thin-walled composite box
295 beams using shear-deformable beam theory, *Eng. Struct.* 30 (2008) 1958–1968.
- [5] A. Varello, E. Carrera, Free vibration response of thin and thick nonhomogeneous shells by refined one-dimensional analysis, *J. Vib. Acoust.* 136 (6) (2014) 061001.
- 300 [6] E. Carrera, M. Filippi, P. K. Mahato, A. Pagani, Advanced models for free vibration analysis of laminated beams with compact and thin-walled open/closed sections, *J. Compos. Mater.* (2014) 0021998314541570.
- [7] V. Giavotto, M. Borri, P. Mantegazza, G. Ghiringhelli, V. Carmaschi, G. Maffioli, F. Mussi, Anisotropic beam theory and applications,
305 *Computers & Structures* 16 (1-4) (1983) 403–413.
doi:10.1016/0045-7949(83)90179-7.
URL <http://www.sciencedirect.com/science/article/B6V28-47S0Y51-1F/2/3dcd227ef680245164977e0448c9f3a6>
- [8] M. Morandini, M. Chierichetti, P. Mantegazza, Characteristic behavior
310 of prismatic anisotropic beam via generalized eigenvectors, *International Journal of Solids and Structures* 47 (10) (2010) 1327–1337.
doi:10.1016/j.ijsolstr.2010.01.017.
URL <http://www.sciencedirect.com/science/article/pii/S0020768310000284>

- 315 [9] P. Masarati, G. L. Ghiringhelli, Characterization of anisotropic,
non-homogeneous plates with piezoelectric inclusions, *Comput-
ers & Structures* 83 (15-16) (2005) 1171–1190. doi:doi:DOI:
10.1016/j.compstruc.2004.10.017.
URL [http://www.sciencedirect.com/science/article/
320 B6V28-4FKY8WG-1/2/c4da0f3cbc7e9cbd655e84b284c805c8](http://www.sciencedirect.com/science/article/B6V28-4FKY8WG-1/2/c4da0f3cbc7e9cbd655e84b284c805c8)
- [10] C. Brillante, M. Morandini, P. Mantegazza, Characterization of beam
stiffness matrix with embedded piezoelectric devices via generalized
eigenvectors, *International Journal of Solids and Structures* 59 (2015)
37–45. doi:10.1016/j.ijsolstr.2015.01.003.
325 URL [//www.sciencedirect.com/science/article/pii/
S0020768315000050](http://www.sciencedirect.com/science/article/pii/S0020768315000050)
- [11] L. Librescu, S. S. Na, Dynamic response of cantilevered thin-walled beams
to blast and sonic-boom loadings, *Shock and Vibration* 5 (1) (1998) 23–33.
- [12] S. Na, L. Librescu, Oscillation control of cantilevers via smart materials
330 technology and optimal feedback control: actuator location and power con-
sumption issues, *Smart Materials and Structures* 7 (6) (1998) 833.
- [13] S. Na, L. Librescu, M.-H. Kim, I.-J. Jeong, P. Marzocca, Robust aeroelastic
control of flapped wing systems using a sliding mode observer, *Aerosp. Sci.
Technol.* 10 (2) (2006) 120–126.
- 335 [14] L. Librescu, S. Na, Z. Qin, B. Lee, Active aeroelastic control of aircraft
composite wings impacted by explosive blasts, *J. Sound Vib.* 318 (1) (2008)
74–92.
- [15] S.-J. Cha, J.-S. Song, H.-H. Lee, S. Na, J.-H. Shim, P. Marzocca, Dynamic
response control of rotating thin-walled composite blade exposed to exter-
340 nal excitations, *J. Aerosp. Eng.* 27 (5) (2014) 04014025.
- [16] A. A. Bent, Active fiber composites for structural actuation, Ph.D. thesis,
Massachusetts Institute of Technology (1997).

- [17] W. K. Wilkie, R. G. Bryant, J. W. High, R. L. Fox, R. F. Hellbaum, A. Jalink Jr, B. D. Little, P. H. Mirick, Low-cost piezocomposite actuator for structural control applications, in: SPIE's 7th Annual International Symposium on Smart Structures and Materials, International Society for Optics and Photonics, 2000, pp. 323–334.
- [18] G. L. Ghiringhelli, P. Masarati, M. Morandini, D. Muffo, Integrated Aeroservoelastic Analysis of Induced Strain Rotor Blades, *Mechanics of Advanced Materials and Structures* 15 (3) (2008) 291. doi:10.1080/15376490801907822.
URL <http://www.informaworld.com/10.1080/15376490801907822>
- [19] C. Brillante, M. Morandini, P. Mantegazza, Periodic controllers for vibration reduction using actively twisted blades, *The Aeronautical Journal* 120 (1233) (2016) 1763–1784. doi:10.1017/aer.2016.80.
URL <https://www.cambridge.org/core/journals/aeronautical-journal/article/div-classtitleperiodic-controllers-for-vibration-reduction-using-actively-twisted-blade/89330CE640F7C750DE4FF561D31DF3D4>
- [20] L. Librescu, O. Song, Behavior of thin-walled beams made of advanced composite materials and incorporating non-classical effects, *Appl. Mech. Rev.* 44 (11) (1991) S174–80.
- [21] L. Librescu, A. Khdeir, Aeroelastic divergence of swept-forward composite wings including warping restraint effect, *AIAA journal* 26 (11) (1988) 1373–1377.
- [22] Z. Qin, L. Librescu, Dynamic aeroelastic response of aircraft wings modeled as anisotropic thin-walled beams, *Journal of Aircraft* 40 (3) (2003) 532–543.
- [23] Z. Qin, L. Librescu, P. Marzocca, Aeroelasticity of composite aerovehicle wings in supersonic flows, *Journal of spacecraft and rockets* 40 (2) (2003) 162–173.

- [24] J.-S. Song, J. Choo, S.-J. Cha, S. Na, Z. Qin, Robust aeroelastic instability suppression of an advanced wing with model uncertainty in subsonic compressible flow field, *Aerosp. Sci. Technol.* 25 (1) (2013) 242–252.
- [25] J. Yang, An introduction to the theory of piezoelectricity, Vol. 9, Springer
375 Science & Business Media, 2004.
- [26] X. Wang, Z. Qin, Nonlinear modal interactions in composite thin-walled beam structures with simultaneous 1: 2 internal and 1: 1 external resonances, *Nonlinear Dynamics* 86 (2) (2016) 1381–1405.
- [27] L. Librescu, S. Na, Dynamic response of cantilevered thin-walled beams to
380 blast and sonic-boom loadings, *Shock. Vib.* 5 (1) (1998) 23–33.
- [28] A. Palazotto, P. Linnemann, Vibration and buckling characteristics of composite cylindrical panels incorporating the effects of a higher order shear theory, *Int. J. Solids Struct.* 28 (3) (1991) 341–361.
- [29] E. A. Armanios, A. M. Badir, Free vibration analysis of anisotropic thin-walled closed-section beams, *AIAA journal* 33 (10) (1995) 1905–1910.
385
- [30] R. Chandra, I. Chopra, Experimental-theoretical investigation of the vibration characteristics of rotating composite box beams, *Journal of Aircraft* 29 (4) (1992) 657–664.
- [31] A. J. Du Plessis, Modeling and experimental testing of twist actuated single cell composite beams for helicopter blade control, Ph.D. thesis, Massachusetts Institute of Technology (1996).
390
- [32] J.-S. Park, J.-H. Kim, Analytical development of single crystal macro fiber composite actuators for active twist rotor blades, *Smart Mater. Struct.* 14 (4) (2005) 745.
- [33] L. Librescu, O. Song, *Thin-Walled Composite Beams: Theory and Application*, Springer, New York, 2006, chap.8, pp. 213-232.
395

List of Figures

	1	Geometry of the beam with a rectangular cross-section (CAS lay-up).	5
400	2	Piezo-actuator location.	7
	3	NACA0012 airfoil cross-section.	16
	4	Tip deflection	18
	5	Actuating moment coefficients with single crystal MFC as a function of the ply-angle θ_p in CAS lay-up configuration.	19
405	6	Actuating force coefficients with single crystal MFC as a function of the ply-angle θ_p in CAS lay-up configuration.	19
	7	Beam tip deflections of the TB-subsystem ($\theta_h = 15^\circ$) as a function of the piezo-actuator ply-angle θ_p	21
	8	Beam tip deflections of the TB-subsystem ($\theta_h = 75^\circ$) as a function of the piezo-actuator ply-angle θ_p	21
410	9	Beam tip deflections of BE-subsystem ($\theta_h = 15^\circ$) as a function of the piezo-actuator ply-angle θ_p	22
	10	Beam tip deflections of BE-subsystem ($\theta_h = 75^\circ$) as a function of the piezo-actuator ply-angle θ_p	23
415	11	Damping ratios as a function of piezo-composite ply-angle θ_p ; bending control methodology, $k_i = 100$, $\theta_h = 15^\circ$	25
	12	Damping ratios as a function of the piezo-composite ply-angle θ_p ; bending control methodology, $k_i = 100$, $\theta_h = 75^\circ$	26
	13	Damping ratios as a function of piezo-composite ply-angle θ_p ; twist control methodology, $k_i = 100$, $\theta_h = 75^\circ$	26
420	14	First four modes frequencies as a function of host structure ply-angle θ_h ; $\theta_p = 120^\circ$ and $k_i = 100$	27
	15	Damping ratio as a function of the host structure ply-angle θ_h , bending control methodology; $\theta_p = 120^\circ$ and $k_i = 100$	28
425	16	Damping ratio as a function of host structure ply-angle θ_h ; twist control methodology, $\theta_p = 120^\circ$ and $k_i = 100$	28

17	Absolute value of the real part of 1TB eigenvalue as a function of the host structure ply-angle θ_h ; $\theta_p = 120^\circ$, $k_i = 100$	30
18	Absolute value of the real part of 2TB, 3TB and 4TB eigenvalues as a function of the host structure ply-angle θ_h ; $\theta_p = 120^\circ$, $k_i = 100$	30
430		
19	Tip flapping displacement \hat{w}_0 in TB-subsystem ($\theta_h = 75^\circ$) subject to an impulse load; $k_i = 100$	31
20	Tip twist rotation $\hat{\phi}$ in TB-subsystem ($\theta_h = 75^\circ$) subject to an impulse load; $k_i = 100$	31
435		
21	Position and size of the piezo-actuator.	32
22	Damping ratios as a function of the piezo-actuator position; $\theta_h = 75^\circ$, $\theta_p = 135^\circ$, $k_i = 100$	33
23	Damping ratios as a function of the piezo-actuator position; $\theta_h = 75^\circ$, $\theta_p = 135^\circ$, $k_i = 100$	33

440 **List of Tables**

	1	Details of thin-walled composite box beam for validation [30] . . .	15
	2	Natural frequency (Hz) for $[45]_6$ CAS lay-up configuration	15
	3	Material properties of E-glass, AFC and single crystal MFC (S- MFC)	17
445	4	Material property and geometric specification of the host struc- ture [33, p. 131]	17
	5	Lay-up configurations for beam with CAS lay-up [unit:deg]. . . .	18